A Generalized Ising-like Model for Spin Crossover Nanoparticles

Catherine Cazelles, Jorge Linares, Pierre-Richard Dahoo, Kamel Boukheddaden

magnetochemistry

MDPI

Article

A Generalized Ising-like Model for Spin Crossover Nanoparticles

Catherine Cazelles [1], Jorge Linares [2,3,*], Pierre-Richard Dahoo [4] and Kamel Boukheddaden [2,*]

[1] Université Paris-Saclay, UVSQ, IUT de Mantes en Yvelines, 78200 Mantes la Jolie, France; catherine.cazelles@uvsq.fr
[2] Université Paris-Saclay, UVSQ, CNRS, GEMAC, 78000 Versailles, France
[3] Departamento de Ciencias, Sección Física, Pontificia Universidad Católica del Perú, Lima 15088, Peru
[4] Université Paris-Saclay, UVSQ, CNRS, LATMOS, 78290 Guyancourt, France; pierre.dahoo@uvsq.fr
* Correspondence: jorge.linares@uvsq.fr (J.L.); kamel.boukheddaden@uvsq.fr (K.B.)

Abstract: Cooperative spin crossover (SCO) materials exhibit first-order phase transitions in the solid state, between the high-spin (HS) and low-spin (LS) states. Elastic long-range interactions are the basic mechanism for this particular behavior and are described well by the Ising-like model, which allows the reproduction of most of the experimental results in the literature. Until now, this model has been applied with an interaction parameter between the molecules, which is considered to be independent of the states. In this contribution, we extend the Ising-like model to include interaction energy that depends on the spin states and apply it to study SCO nanoparticles. Our research shows that following this new hypothesis, the equilibrium temperature shifts toward higher values.

Keywords: nanoparticles; spin crossover; phase transition; Monte Carlo simulations; Ising model

Citation: Cazelles, C.; Linares, J.; Dahoo, P.-R.; Boukheddaden, K. A Generalized Ising-like Model for Spin Crossover Nanoparticles. *Magnetochemistry* **2022**, *8*, 49. https://doi.org/10.3390/magnetochemistry8050049

Academic Editor: Zoi G. Lada

Received: 14 March 2022
Accepted: 7 April 2022
Published: 4 May 2022

1. Introduction

Spin crossover (SCO) nanoparticles [1–12] are composed of transition metals with configurations ranging from $3d^4$ to $3d^8$ embedded in an organic matrix. They are characterized by two different electronic spin configurations, resulting in two stable, magnetic macrostates, termed high spin (HS) and low spin (LS). LS-HS transitions are triggered by an external constraint. Most of the SCO compounds that have been studied are based on the Fe (II) $3d^6$ configuration. For the $3d^8$ case (Ni^{2+} SCO) and following the work of O.A. Qamar et al. [13], the SCO phenomenon is associated with three different lattice distortions, one of them being from a square planar (LS, S = 0) to a tetrahedral geometry (HS, S = 1).

When a Fe (II) cation coordinates in an octahedral ligand field (O_h) as a metal complex, the degenerated orbitals of the cation split into triply degenerate t_{2g} and doubly degenerate e_g states. The macrostates are related to the micro-configurations permitted by the distribution of the six electrons in the t_{2g} and e_g states, mediated by the competition between the pairing electron affinity and the strength of the ligand field, which defines the energy gap between the states. The LS state corresponds to the limiting strong field ligand case, which favors the pairing of the six electrons in the t_{2g} orbitals ($t_{2g}^6 e_g^0$ and spin S = 0), and the HS state corresponds to the limiting weak field ligand case, which allows the distribution of the electrons on both the t_{2g} and e_g states within the frame of Hund's rule ($t_{2g}^4 e_g^2$ and total spin S = 2). The LS state is thus diamagnetic when neglecting the second-order Zeeman effect, and the SCO appears in a deeply colored state, while the HS state is a paramagnetic, fainter-colored state. On top of that, the Fe-ligand distance is greater in the HS state compared to the LS state.

The change in spin state can thus be observed through significant changes, such as color, volume, magnetic state and electrical conductivity of the compound from a variety of characterization techniques, including: magnetometry [14,15], Mössbauer spectroscopy [16], optical spectroscopy [17], ellipsometry [18], X-ray diffraction [15,19], calorimetry [20,21], diffuse reflectance [22,23], Raman [15], etc.

From Mössbauer studies, the Debye temperature is observed to be higher for the LS phase than for the HS state. Accordingly, this result suggests that the interactions between the metal complex sites, which are in the LS state, are stronger than those pertaining to interacting HS state sites. This result is in line with a greater HS state Fe-ligand distance. Following these experimental results and conclusions, the theoretical work presented in this contribution is based on an Ising-like model [24–28] that is built on three different coupling parameters to simulate the thermodynamic properties of a SCO solid. Thus, three interaction parameters were introduced: J_{LL} when the two interacting sites are in the LS state, J_{HH} when they are in the HS state and J_{HL} when one site is in the HS state and the other is in the LS state. In the first step, to reduce the number of parameters, the J_{HL} was taken as the average value of the J_{LL} and J_{HH}. Then, the effect of the three different interaction parameters on the equilibrium temperature, as well as on the hysteresis width, were analyzed.

This generalized Ising-like model is presented in Section 2, and the Monte Carlo entropic sampling simulations used to calculate the density of the states are developed in Section 3. The results and analysis are summarized in Section 4.

2. The Model

In the "classical" Ising-like model [24,25], the spin crossover molecules are described by the fictitious operator σ, which has two eigenvalues: +1 assigned to the HS state (with a degeneracy g_{HS}) and -1 to the LS state (with a degeneracy g_{LS}). The Hamiltonian for N-isolated molecules is written as:

$$H = \frac{\Delta}{2} \sum_{i=1}^{N} \sigma_i \tag{1}$$

where Δ is the gap between the fundamental energies of the HS and LS states. Considering the different degeneracies (g_{HS} and g_{LS}) between the respective HS and LS states arising from their different spin values and phonon spectra, the Hamiltonian is isomorphic to:

$$H = \frac{\Delta - k_B T \ln(g)}{2} \sum_{i=1}^{N} \sigma_i \tag{2}$$

with $g = \frac{g_{HS}}{g_{LS}}$, where T is the temperature and k_B is the Boltzmann constant.

To account for the interaction between the molecules, an interaction potential energy, written under an Ising form, is added to the previous Hamiltonian, such that:

$$H = \frac{\Delta - k_B T \ln(g)}{2} \sum_{i=1}^{N} \sigma_i - \sum_{i,j} J_{ij} \sigma_i \sigma_j \tag{3}$$

and considering the presence of short (J) and long-range (G) interactions, as proposed by Linares et al. [26] and demonstrated later in true elastic models by M. Paez-Espejo et al. [29], the Hamiltonian is finally expressed as

$$H = \frac{\Delta - k_B T \ln(g)}{2} \sum_{i=1}^{N} \sigma_i - \sum_{\langle i,j \rangle} J_{ij} \sigma_i \sigma_j - \sum_{i=1}^{N} \sigma_i G \langle \sigma \rangle \tag{4}$$

which re-writes as

$$H = \frac{\Delta - k_B T \ln(g) - G\langle \sigma \rangle}{2} \sum_{i=1}^{N} \sigma_i - \sum_{\langle i,j \rangle} J_{ij} \sigma_i \sigma_j \tag{5}$$

where the long-range interaction (G) is treated in the mean-field approximation. It is worth remarking that in this contribution, to reduce the parameters, we do not consider different long-range interactions for HS and LS species.

We notice in Equation (5) that the interaction term $J_{ij} = J$ for the nearest molecules (four in the square lattice, six in the cubic lattice) is considered to be independent of the spin states in the "classical" Ising-like model.

In this contribution, we generalize the previous Ising-like model and consider that the short-range interaction term J_{ij} between the sites σ_i and σ_j depends on their spin states. So, three interaction constants are introduced:

J_{HH} if both molecules are HS, $\sigma_i = \sigma_j = +1$;
J_{LL} if both molecules are LS, $\sigma_i = \sigma_j = -1$;
J_{HL} if one molecule is HS and the other LS, $\sigma_i = -\sigma_j = \pm 1$.
For the sake of simplicity, it is assumed that $J_{HL} = \frac{J_{HH}+J_{LL}}{2}$.
Using the following parameters:

$$m = \sum_{i=1}^{N} \sigma_i,\ s = \sum_{\langle i,j \rangle} \sigma_i \sigma_j \text{ and } h = -\frac{\Delta - k_B T \ln(g) - G\langle \sigma \rangle}{2} \tag{6}$$

Hamiltonian (5) writes as:

$$H = -h\, m\ -\ J_{HH}\, s_{HH}\ -\ J_{HL}\, s_{HL} - J_{LL}\, s_{LL} \tag{7}$$

where the two-sites' correlations s_{HH}, s_{LL} and s_{LL} write:

$$\begin{array}{c} s_{HH} = N_{++} = \sum_{\langle i,j \rangle} \sigma_i \sigma_j,\ \text{for } \sigma_i = \sigma_j = +1 \\ s_{LL} = N_{--} = \sum_{\langle i,j \rangle} \sigma_i \sigma_j,\ \text{for } \sigma_i = \sigma_j = -1 \\ s_{HL} = N_{+-} + N_{-+} = \sum_{\langle i,j \rangle} \sigma_i \sigma_j,\ \text{for } \sigma_i = -\sigma_j = \pm 1 \end{array} \tag{8}$$

Here, N_{++}, N_{--} and N_{+-} are the numbers of the HS-HS, LS-LS and HS-LS nearest neighbor configurations, respectively, which fulfill the relation $N_{++} + N_{--} + 2N_{+-} = 2N$, where N is the total number of sites in the considered 2D lattice.

The partition function is then given as a function of these macroscopic variables by:

$$Z = \sum_{1}^{N'} \mathrm{d}(\mathrm{m}, s_{HH}, s_{HL},\ s_{LL}) \exp(-\beta\ (-h\, m - J_{HH} s_{HH} - J_{HL} s_{HL} - J_{LL} s_{LL})) \tag{9}$$

where $\beta = \frac{1}{k_B\, T}$ and $\mathrm{d}(\mathrm{m}, s_{HH}, s_{HL},\ s_{LL})$, obtained by the Monte Carlo entropic sampling method (MCES, see Section 3), is the number of configurations with the same m, s_{HH}, s_{HL} and s_{LL} values. N' is the total number of macrostates characterized by these m, s_{HH}, s_{HL} and s_{LL} values.

The thermal average value of the operator $\langle \sigma, (T) \rangle$, denoted $\langle \sigma \rangle$, is given by the following relation:

$$\langle \sigma \rangle = \frac{\sum_{1}^{N'} m\ \ \mathrm{d}(\mathrm{m}, s_{HH}, s_{HL},\ s_{LL}) \exp(-\beta\ (-h\, m - J_{HH} s_{HH} - J_{HL} s_{HL} - J_{LL} s_{LL})\ )}{Z} \tag{10}$$

which is related to the high-spin fraction (Nhs) by the expression:

$$Nhs = \frac{1 + \langle \sigma \rangle}{2} \tag{11}$$

Equation (10) is solved using the bisection technique.

3. Entropic Sampling

The purpose of the Monte Carlo entropic sampling method (MCES) [30–32] is to obtain the density of the states $\mathrm{d}(\mathrm{m}, s_{HH}, s_{HL},\ s_{LL})$ in an attempt to scan the entire space of configurations. To achieve this, the idea is to introduce in the detailed balance equation:

$$P_i\, W_{i \to j} = P_j\ \ W_{j \to i} \tag{12}$$

P_i the probability of obtaining the macrostate $(\mathrm{m}, s_{HH}, s_{HL},\ s_{LL})$, shown as:

$$P_i = \frac{1}{d(m_i,\ (s_{HH})_i,\ (s_{HL})_i,\ (s_{LL})_i)} \tag{13}$$

$W_{i\to j}$ is the transition probability from the macrostate (i), characterized by m_i, $(s_{HH})_i$, $(s_{HL})_i$, $(s_{LL})_i$, to the macrostate (j).

Such a choice of P_i favors the macrostates with a small density of states and dampens those with a high density.

The detailed balance equation is then expressed as:

$$\begin{array}{c} P_{(m_i,\ (s_{HH})_i,\ (s_{HL})_i,\ (s_{LL})_i)}\ W_{(m_i,\ (s_{HH})_i,\ (s_{HL})_i,\ (s_{LL})_i)\to(m_j,\ (s_{HH})_j,\ (s_{HL})_j,\ (s_{LL})_j)} = \\ P_{(m_j,\ (s_{HH})_j,\ (s_{HL})_j,\ (s_{LL})_j)}\ W_{(m_j,\ (s_{HH})_j,\ (s_{HL})_j,\ (s_{LL})_{j\to}(m_i,\ (s_{HH})_i,\ (s_{HL})_i,\ (s_{LL})_i))} \end{array} \tag{14}$$

Using $d(m_i,\ (s_{HH})_i,\ (s_{HL})_i,\ (s_{LL})_i)$ as a bias, a "Monte Carlo step" run and a histogram of the frequency of the macrostates $H(m_i,\ (s_{HH})_i,\ (s_{HL})_i,\ (s_{LL})_i)$ are obtained. Then, the density of states in the next "Monte Carlo step" is improved by the following relation:

$$\begin{array}{c} d\left(m_{i+1},\ (s_{HH})_{i+1},\ (s_{HL})_{i+1},\ (s_{LL})_{i+1}\right) = \\ H(m_i,\ (s_{HH})_i,\ (s_{HL})_i,\ (s_{LL})_i) \times d(m_i,\ (s_{HH})_i,\ (s_{HL})_i,\ (s_{LL})_i) \end{array} \tag{15}$$

This technique is used iteratively until an almost constant (flat) $H(m_i, (s_{HH})_i, (s_{HL})_i, (s_{LL})_i)$ histogram is obtained.

The density of states is then used to calculate the thermal average value of the fictitious spin operator.

4. Numerical Results and Analysis

In the calculations, a set of realistic thermodynamic parameters derived from experimental data on the prototype SCO complex $[Fe(btr)_2(NCS)_2]$, *btr* = 4,4′-*bis*-1,2,4-*triazole* [16] is used. From the enthalpy H measurements, we derived the value of the energy gap as Δ/k_B = 1300 K. The equilibrium temperature T_{eq} is deduced from the evolution of ΔH and is fixed at 216.3 K, from which the entropy ΔS = $\Delta H/T_{eq}$ is calculated to be ΔS= 50 J/K/mol. Recall that according to the previous model, the expression of T_{eq} is given by $T_{eq} = \frac{\Delta}{k_B \ln(g)}$.

To study the behavior of SCO molecules, the following definitions are used such that T_{up} is the ascending thermal transition temperature, T_{down} is the descending thermal transition temperature and $T_{eq} = T_{1/2}$ is the average temperature between T_{up} and T_{down} in which the HS fraction is equal to 1/2. The hysteresis width is defined as $\Delta T = T_{up} - T_{down}$.

In the first part, we study the effect of the interaction parameters on the occurrence of thermal hysteresis and the behavior of its width when it exists. It is worth mentioning that from the experimental point of view, the control of the interactions is usually attempted through metal dilution by replacing a fraction of Fe (II) active SCO atoms with Co, Ni or Zn ions [21,33,34]. Unfortunately, it is usually observed that the effect of the dopant not only breaks down the interactions as expected, but also modulates the ligand field. The results concerning the size effect are given in the second and last parts.

- *Effect of the Interaction Parameters*

The effect of the interaction is then simulated by monitoring the value of the effective interaction parameter J/k_B.

This "average" interaction parameter is defined here as the usual J parameter of the "classical" Ising-like model, and so it relates to J_{HH}, J_{HL} and J_{LL} by the following relation:

$$-J\,s = -J_{HH}\,s_{HH} - J_{HL}\,s_{HL} - J_{LL}\,s_{LL} \tag{16}$$

where $s = s_{HH} + s_{LL} - 2s_{HL}$.

- The Case $x = J_{HH}/J_{LL} = 1.0$

Since $J_{HL} = \frac{J_{HH}+J_{LL}}{2}$, the case $x = 1$ corresponds to $J_{HH} = J_{LL} = J_{HL}$, which will be denoted for simplicity by J. The evolution of the HS fraction, noted as Nhs, is simulated as a function of the temperature corresponding to different values of the average short-range parameter J. Figure 1 illustrates the thermal behavior of the HS fraction for various J/k_B values ranging from 12 to 25 K.

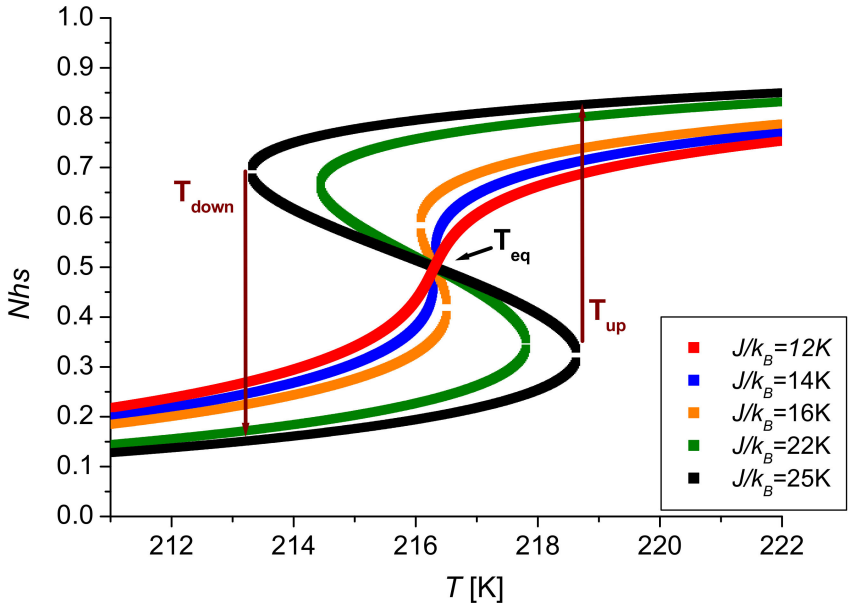

Figure 1. Thermal evolution of the HS fraction in a SCO system with a size of 6×6 for different values of the average interaction parameter J/k_B: $J/k_B = 12$ K (red square), $J/k_B = 14$ K (blue square), $J/k_B = 16$ K (orange square), $J/k_B = 22$ K (green square) and $J/k_B = 25$ K (black square). The computational parameters are: $\Delta/k_B = 1300$ K, $G/k_B = 172.2$ K, $x = J_{HH}/J_{LL} = 1.0$ and $\ln(g) = 6.01$.

The curves obtained for the 6×6 square system show that the nature of the transition (hysteretic, abrupt or gradual) is closely correlated to the intensity of the short-range interactions.

When the average short-range interaction J/k_B is decreased, the thermal hysteresis width reduces from $\Delta T = 5.41$ K ($J/k_B = 25$ K) to $\Delta T = 0.41$ K ($J/k_B = 16$ K) and vanishes below the critical value $J/k_B \simeq 15K$. Below this value, the interactions are not strong enough to produce the collective first-order transition accompanied by the hysteretic behavior, and the system's feature changes into a gradual one, in fair agreement with experimental findings [21,33,34] and previous simulations [26].

Moreover, it can be seen in Figure 1 that when all the interaction parameters J_{HH}/k_B, J_{LL}/k_B and J_{HL}/k_B are equal, the transition temperature T_{eq} is independent of the J/k_B values and remains equal to $T_{eq} = \Delta/(k_B \ln(g)) = 216.3$ K.

The previous results are summarized in Figure 2, where we report the phase diagram of the system in the space coordinates T versus J/k_B. The presented phase diagram clearly highlights the existence of two regions of thermal behavior: a region corresponding to $J/k_B \geq 15$ K in which the system presents a single first-order phase transition, while a gradual transition is observed when $J/k_B < 15$ K.

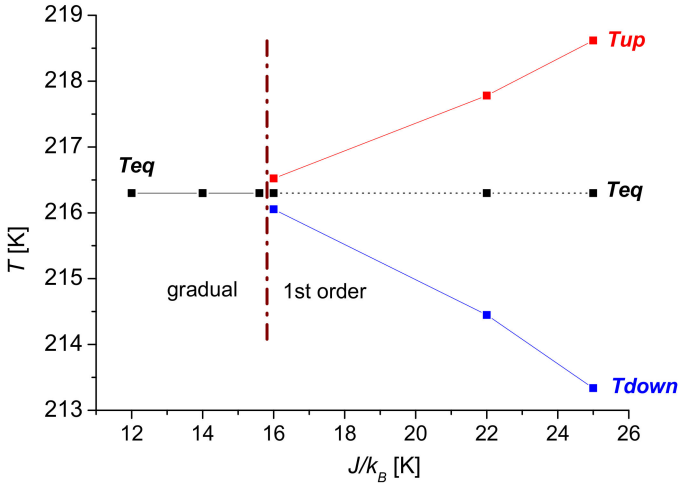

Figure 2. Phase diagram T = f (J/k_B) for a 6 × 6 square lattice. The red and blue squares correspond, respectively, to the upper and lower transitions for the heating (T_{up}) and cooling (T_{down}) temperatures of the thermal HS fraction. The black squares correspond to the equilibrium temperatures (T_{eq}). The computational parameters are: Δ/k_B = 1300 K, G/k_B = 172.2 K, $x = J_{HH}/J_{LL} = 1.0$ and ln(g) = 6.01.

- The Case of $x = J_{HH}/J_{LL}$ = 0.4

The ratio $x = J_{HH}/J_{LL}$ has been set to the value of 0.4, and therefore, the short-range interaction parameters (J_{HH}, J_{HL}, J_{LL}) are different. In order to simulate the dilution effect, the intensity of the average short-range interaction J/k_B is gradually reduced from $J/k_B = 19$ K to $J/k_B = 11$ K.

The obtained curves are plotted in Figure 3 in the case of a 6 × 6 nanoparticle configuration. The values of the thermal hysteresis widths, as well as the equilibrium temperature T_{eq}, are summarized in Table 1 as a function of the J/k_B parameter. The inspection of the thermal behavior of the HS fraction in Figure 3 clearly shows a significant difference compared to Figure 1, which remained symmetric around the invariant value of the transition temperature. Here, the change of the interaction parameter results in a large deformation and shift of $Nhs(T)$, which means that the interaction J affects both the cooperativity and the ligand field energy.

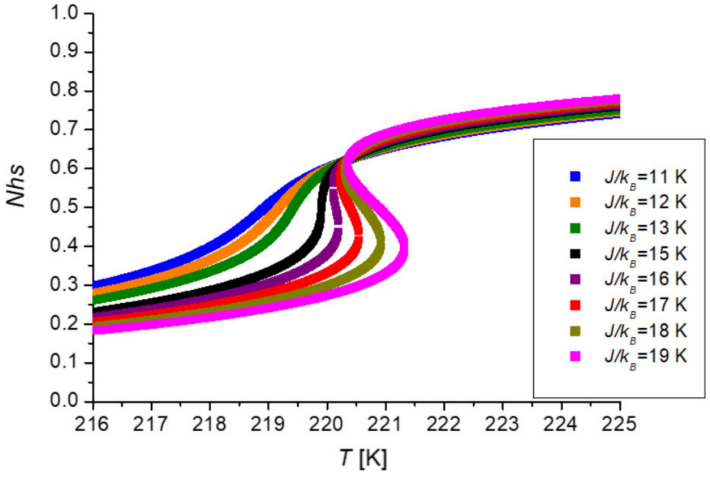

Figure 3. Thermal evolution of the HS fraction in a SCO system with a size of 6 × 6 for different values of the average interaction parameter J/k_B:$J/k_B = 19$ K (magenta square), J/k_B = 18 K (dark yellow square), J/k_B = 17 K (red square), J/k_B = 16 K (purple square), J/k_B = 15 K (black square), $J/k_B = 13$ K (green square), $J/k_B = 12$ K (orange square) and $J/k_B = 11$ K (blue square). The computational parameters are: $\Delta/k_B = 1300$ K, G/k_B = 172.2 K, $x = J_{HH}/J_{LL} = 0.4$ and ln(g) = 6.01.

Table 1. Values of the thermal hysteresis width $\Delta T_{hyst} = T_{up} - T_{down}$ and the equilibrium temperature T_{eq} as a function of J/k_B, J_{HH}/k_B and J_{LL}/k_B in a SCO system with a size of 6 × 6. The computational parameters are: $\Delta/k_B = 1300$ K, $G/k_B = 172.2$ K, $x = J_{HH}/J_{LL} = 0.4$ and ln(g) = 6.01.

J/k_B [K]	J_{HH}/k_B [K]	J_{LL}/k_B [K]	$(J_{LL}-J_{HH})/k_B$ [K]	ΔT_{hyst} [K]	T_{eq} [K]
19	10.86	27.14	16.28	1.03	220.86
18	10.28	25.71	15.43	0.62	220.60
17	9.72	24.29	14.57	0.33	220.37
16	9.14	22.86	13.72	0.10	220.13
15	8.57	21.43	12.86	0	219.90
13	7.43	18.58	11.15	0	219.43
12	6.85	17.14	10.29	0	219.18
11	6.28	15.71	9.42	0	218.93

As can be seen in Table 1, when the interaction parameter J decreases, the values of J_{HH}/k_B and J_{LL}/k_B also decrease; the gap $(J_{LL} - J_{HH})/k_B$ decreases as well. An important result is that, at the same time, the thermal hysteresis width decreases, and the equilibrium temperature of the system is shifted to lower temperatures.

In Figure 4, we plot the variations of T_{up}, T_{down} and T_{eq} *versus* J/k_B, which leads to the system's phase diagram in the (T, J/k_B) variables' space, highlighting the existence of two regions of thermal behavior. The thermal hysteresis loop (~1.03 K wide for $J/k_B = 19$ K), associated with a single first-order phase transition, rapidly narrows when decreasing J/k_B and collapses at the threshold value $(J/k_B)_c \approx 16$ K. These results agree qualitatively with Mössbauer spectroscopy and magnetic measurements realized on iron (II)-based SCO materials diluted with high-spin cobalt (II) ions [33,34]. There, the Co has a double role: it breaks down the interactions between the Fe (II) SCO species and also affects the ligand field energy through steric effects.

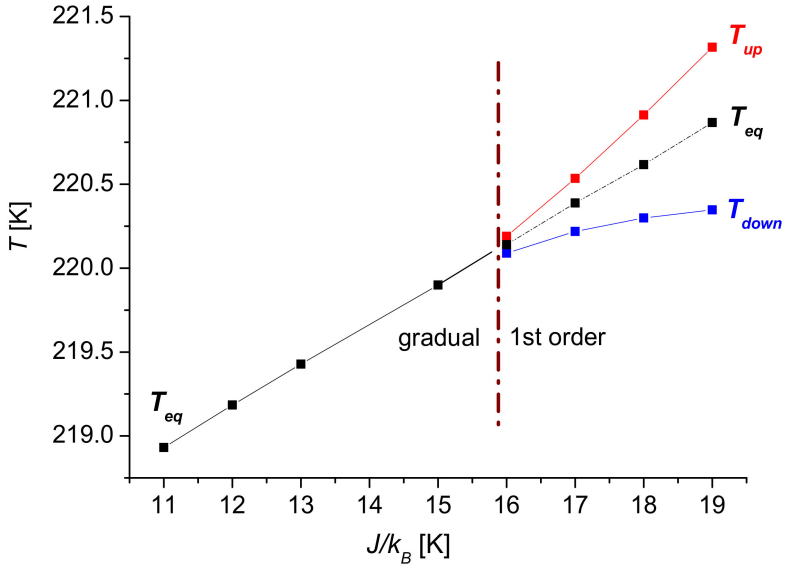

Figure 4. Temperature T versus J/k_B for a 6 × 6 square lattice. The red (T_{up}) and blue (T_{down}) squares correspond, respectively, to the transition temperatures of the upper and lower branches of thermal hysteresis. The black squares correspond to the equilibrium temperatures (T_{eq}) of the gradual transition region. The computational parameters are: Δ/k_B = 1300 K, G/k_B = 172.2 K, $x = (J_{HH}/k_B)/(J_{LL}/k_B) = 0.4$ and ln(g) = 6.01.

Linear regression in the $T_{eq}(J/k_B)$ variation gives: $T(J/k_B) = 0.24072 \times J/k_B + 216.30$.

Figure 5 shows the thermal evolution of the HS fraction in the case of a 10 × 10 square lattice. The results are also reported in Table 2. The comparaison of the simulation for 6 × 6 and 10 × 10 square lattices are given in Table 3.

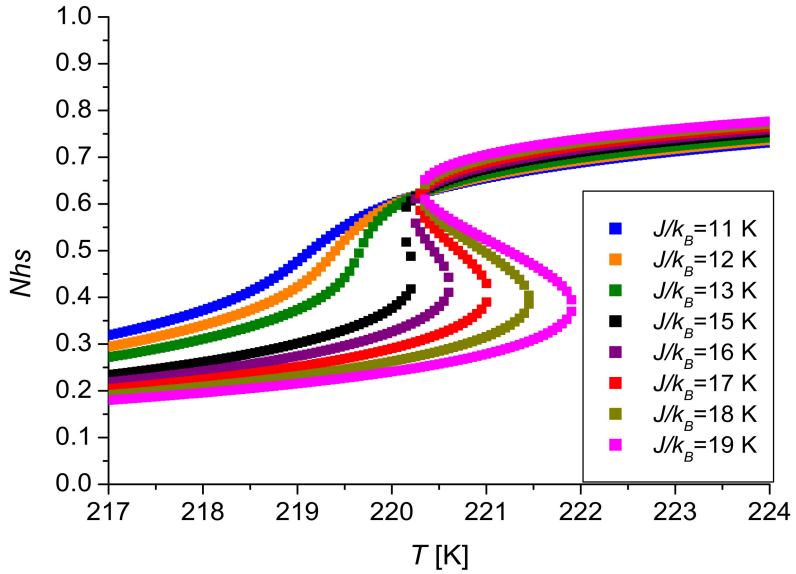

Figure 5. Thermal evolution of the HS fraction in a SCO system with a size of 10 × 10 for different values of the average interaction parameter J/k_B:J/k_B = 19 K (magenta square), J/k_B = 18 K (dark yellow square), J/k_B = 17 K (red square), J/k_B = 16 K (purple square), J/k_B = 15 K (black square), J/k_B = 13 K (green square), J/k_B = 12 K (orange square), J/k_B = 11 K (blue square). The computational parameters are: Δ/k_B = 1300 K, G/k_B = 172.2 K, $x = J_{HH}/J_{LL}$ = 0.4 and ln(g) = 6.01.

Table 2. Evolution of the thermal hysteresis width, $\Delta T_{hyst} = T_{up} - T_{down}$, and the equilibrium temperature, T_{eq}, as a function of J/k_B, J_{HH}/k_B and J_{LL}/k_B in a SCO system with a size of 10 × 10. The computational parameters are: Δ/k_B = 1300 K, G/k_B = 172.2 K, $x = J_{HH}/J_{LL}$ and ln(g) = 6.01.

J/k_B [K]	J_{HH}/k_B [K]	J_{LL}/k_B [K]	($J_{LL}/k_B - J_{HH}/k_B$) [K]	ΔT_{hyst} [K] 10 × 10	T_{eq} [K] 10 × 10
19	10.837	27.094	16.257	1.57	221.244
18	10.267	25.669	15.402	1.13	220.941
17	9.697	24.244	14.547	0.71	220.709
16	9.125	22.814	13.689	0.38	220.463
15	8.555	21.389	12.834	0.09	220.160
13	7.415	18.539	11.124	0	219.658
12	6.845	17.114	10.269	0	219.409
11	6.274	15.685	9?411	0	219.149

Table 3. Comparison of simulations for the 6 × 6 and 10 × 10 lattices.

J/k_B [K]	ΔT_{hyst} [K] 6 × 6	T_{eq} [K] 6 × 6	ΔT_{hyst} [K] 10 × 10	T_{eq} [K] 10 × 10
19	1.03	220.86	1.57	221.244
18	0.62	220.60	1.13	220.941
17	0.33	220.37	0.71	220.709
16	0.10	220.13	0.38	220.463
15	0	219.90	0.09	220.160
13	0	219.43	0	219.658
12	0	219.18	0	219.409
11	0	218.93	0	219.149

The transition temperatures reported in Figure 6, in the heating mode (T_{up}) and in the cooling mode (T_{down}), clearly show that the width of the hysteresis loop $\Delta T = T_{up} - T_{down}$ increases when the J/k_B interaction is stronger. Linear regression leads for the Teq Branch to: $T(J/k_B) = 0.26019 \times J/k_B + 216.30$.

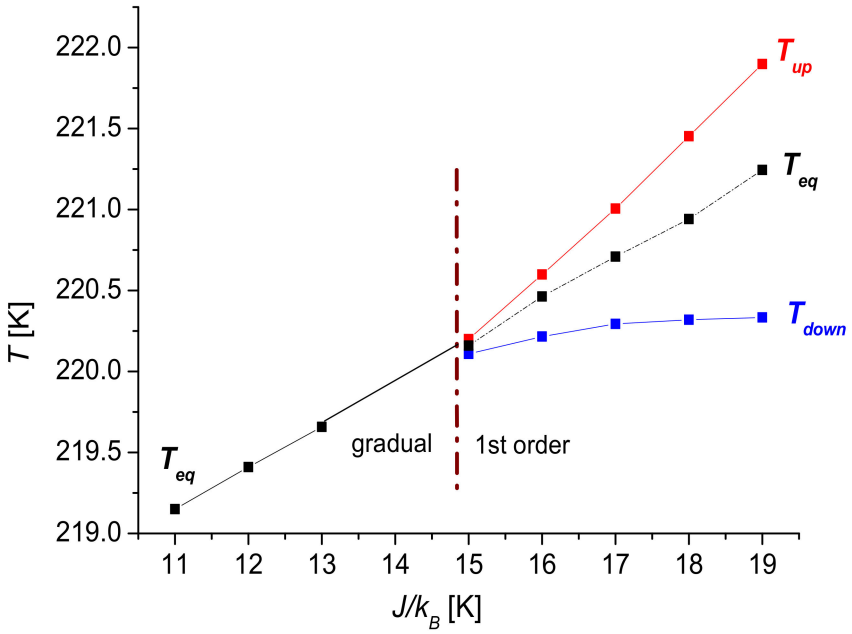

Figure 6. Phase diagram T = f (J/k_B) for a 10 × 10 square lattice. The red and blue squares correspond, respectively, to the upper and lower transitions for the heating (T_{up}) and cooling (T_{down}) temperatures of the thermal HS fraction. The black squares correspond to the equilibrium temperatures (T_{eq}). The computational parameters are: Δ/k_B = 1300 K, G/k_B = 172.2 K, $x = (J_{HH}/J_{LL}) = 0.4$ and ln(g) = 6.01.

- *Effects of the Variation of $x = J_{HH}/J_{LL}$*

In the following, the value of the ratio x is gradually decreased in the interval [1.0: 0.2]. The value of the J/k_B parameter is set to 14.8 K in all simulations. As can be seen in Table 4, when the ratio $x = J_{HH}/J_{LL}$ decreases, the difference between J_{HH}/k_B and J_{LL}/k_B increases, and the J_{LL}/k_B value increases while that of J_{HH}/k_B decreases.

Table 4. Equilibrium temperatures and hysteresis widths calculated for different values of $x = J_{HH}/J_{LL}$ parameter in a 6 × 6 square lattice. The computational parameters are: Δ/k_B = 1300 K, J/k_B = 14.8 K, G/k_B = 172.2 K and ln(g) = 6.01.

J/k_B [K]	x	J_{LL}/k_B [K]	J_{HH}/k_B [K]	J_{HL}/k_B [K]	ΔT_{hyst} [K]	T_{eq} [K]
14.8	1.0	14.8	14.8	14.8	0.11	216.30
14.8	0.6	18.5	11.09	14.8	0	218.38
14.8	0.2	24.66	4.93	14.8	0	221.85

The results reported in Figure 7 for a 6 × 6 system show that the decrease in x progressively shifts the equilibrium temperature T_{eq} toward higher values. The equilibrium temperature, which is equal to 216.3 K when x = 1, reaches the value of 221.85 K when $x = 0.2$. The values of the equilibrium temperatures associated with the different x values are reported in the last column of Table 4.

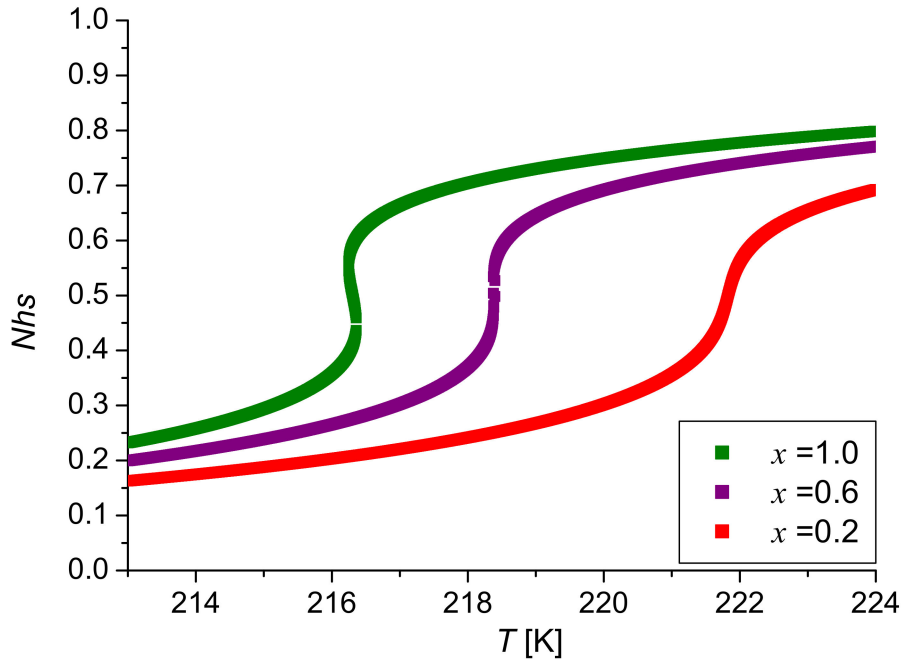

Figure 7. Thermal evolution of the HS fraction in a SCO system with a size of 6 × 6 for different values of the x parameter: x = 1.0 (green square), x = 0.6 (purple square) and x = 0.2 (red square). The computational parameters are: Δ/k_B = 1300 K, J/k_B = 14.8 K, G/k_B = 172.2 K and ln(g) = 6.01.

In this section, the size effect is analyzed, and calculations are performed in the case of a 10 × 10 square lattice. In the same way, for the 6 × 6 lattice, the value of the ratio x is gradually decreased from the value of 1.0 to the value of 0.2. The results are summarized in Table 5 and in Figure 8 for parameter J/k_B set to 14.8 K.

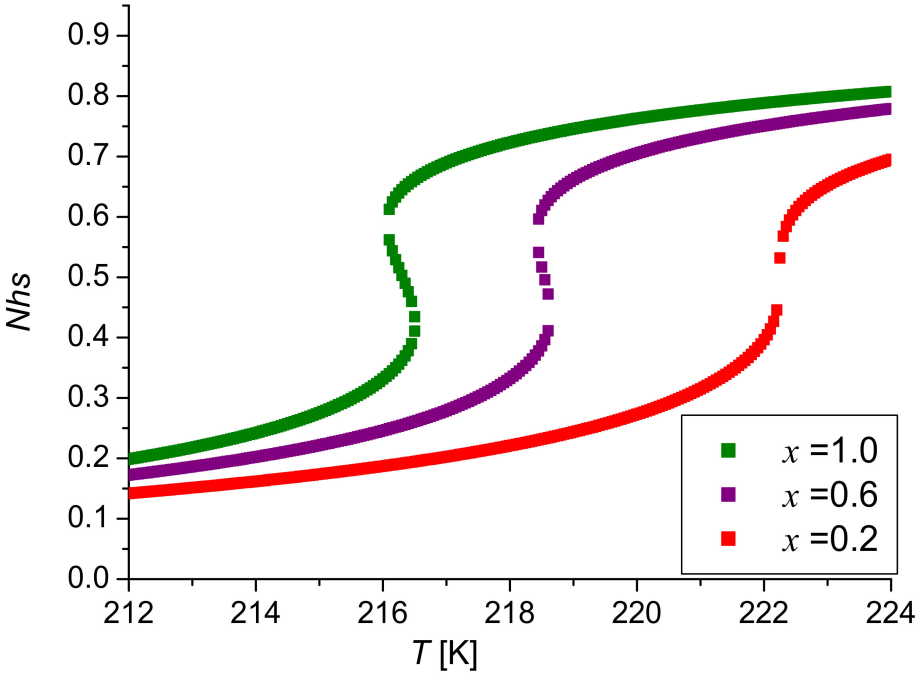

Figure 8. Thermal evolution of the HS fraction in a SCO system with a size of 10 × 10 for different values of the x parameter: x = 0.2 (red square), x = 0.6 (purple square) and x = 1.0 (green square). The computational parameters are: Δ/k_B = 1300 K, J/k_B = 14.8 K, G/k_B = 172.2 K and ln(g) = 6.01.

Table 5. Equilibrium temperatures and hysteresis widths calculated for different values of the $x = (J_{HH}/k_B)/(J_{LL}/k_B)$ parameter in a 10 × 10 square lattice. The computational parameters are: Δ/k_B = 1300 K, J/k_B = 14.8 K, G/k_B = 172.2 K and ln(g) = 6.01.

J/k_B [K]	x	J_{LL}/k_B [K]	J_{HH}/k_B [K]	J_{HL}/k_B [K]	ΔT_{hyst} [K]	T_{eq} [K]
14.8	1.0	14.8	14.8	14.8	6.10	216.30
14.8	0.6	18.48	11.087	14.78	5.16	219.88
14.8	0.2	24.59	4.92	14.75	0	222.29

The results of the 10 × 10 lattice are qualitatively similar to those obtained for the 6 × 6 nanoparticle configuration. When the value of the x ratio decreases, the difference between J_{HH}/k_B and J_{LL}/k_B increases; the interactions between molecules in the LS states (J_{LL}/k_B) are much stronger than those in the HS state (J_{HH}/k_B), and the system remains in an LS configuration for a longer temperature interval. The equilibrium temperature T_{eq} gradually moves toward the order-disorder temperature $T_{O.D.}$. The hysteresis width decreases and vanishes for weaker J/k_B values when T_{eq} becomes greater than $T_{O.D.}$.

5. Conclusions

In this study, the behavior of 2D-SCO nanostructures is analyzed with particular attention to the effect of the short-range interactions involved in the model. Indeed, three coupling terms were considered (i) J_{HH}/k_B between two HS molecules, (ii) J_{LL}/k_B between two LS molecules and (iii) $J_{HL}/k_B = J/k_B$ between a molecule in the HS state and another one in the LS state with $J/k_B = (J_{HH}/k_B + J_{LL}/k_B)/2$.

The J_{HH}/J_{LL} ratio effect is parametrized by x. When $x = 1$, which corresponds to the case where the three short-range interactions are equal, the equilibrium temperature of the system T_{eq} remains constant. The nature of the transition from LS to HS configuration is governed by the intensity of the interactions and, therefore, the value of the J/k_B and G/k_B parameters. Increasing the short-range interaction parameter J/k_B leads to a hysteretic transition. This behavior is explained by the fact that the Curie (or the order-disorder) temperature designed by $T_{O.D.}$ increases. When x is set to a value other than 1, a "pseudo-dilution" effect is simulated by gradually reducing J/k_B. Figures 4 and 6 highlight that the equilibrium temperature shows a linear decrease towards $\Delta/(k_B \ln(g))$ = 216.3 K. Moreover, the hysteretic behavior vanishes at a threshold value of $J_c/k_B \approx 16K$ and $J_c/k_B \approx 15K$ for 6 × 6 and 10 × 10 systems, respectively. This feature is connected to the relative positions of T_{eq} and $T_{O.D.}$ and can be explained by the fact that the order-disorder transition $T_{O.D.}$ decreases faster for small lattices. The condition $T_{eq} > T_{O.D.}$ leads to a gradual transition. In the present study, we mainly focused on the effect of varying x when J/k_B is constant. An important result is that when the difference between J_{HH}/k_B and J_{LL}/k_B is increased, the LS state is stabilized and T_{eq} is shifted toward higher temperatures. This behavior is more significant for larger lattices. The effects of the interactions between surface molecules and their environment will also be explored in future work.

Author Contributions: J.L. and K.B. proposed the model, C.C. and J.L. calculated the density of states and conducted the simulations, J.L., K.B., C.C. and P.-R.D. analyzed the results. All the authors participated in writing the paper. All authors have read and agreed to the published version of the manuscript.

Funding: This research received no external funding.

Institutional Review Board Statement: Not applicable.

Informed Consent Statement: Not applicable.

Data Availability Statement: Not applicable.

Acknowledgments: This research was funded by the CNRS and the Université de Versailles St-Quentin member of the Université Paris-Saclay, the ANR project Mol-CoSM No. ANR-20-CE07-

0028-02 and the French–Japan international laboratory (LIA IM-LED). We thank all of them for their financial support.

Conflicts of Interest: The authors declare no conflict of interest.

References

1. Coronado, E. Molecular magnetism: From chemical design to spin control in molecules, materials and devices. *Nat. Rev. Mater.* **2020**, *5*, 87–104. [CrossRef]
2. Gütlich, P.; Hauser, A.; Spiering, H. Thermal and optical switching of Iron(II) Complexes. *Angew. Chem.* **1994**, *33*, 2024–2054. [CrossRef]
3. Sanvito, S. Molecular Spintronics. *Chem. Soc. Rev.* **2011**, *40*, 3336–3355. [CrossRef] [PubMed]
4. Decurtins, S.; Gütlich, P.; Köhler, C.P.; Spiering, H.; Hauser, A. Light-induced excited spin state trapping in a transition-metal complex: The hexa-1-propyltetrazole-iron (II) tetrafluoroborate spin-crossover system. *Chem. Phys. Lett.* **1984**, *105*, 1–4. [CrossRef]
5. Linares, J.; Codjovi, E.; Garcia, Y. Pressure and Temperature Spin Crossover Sensors with Optical Detection. *Sensors* **2012**, *12*, 4479–4492. [CrossRef]
6. Boukheddaden, K.; Ritti, M.H.; Bouchez, G.; Sy, M.; Dîrtu, M.M.; Parlier, M.; Linares, J.; Garcia, Y. Quantitative contact pressure sensor based on spin crossover mechanism for civil security applications. *J. Phys. Chem. C* **2018**, *122*, 7597–7604. [CrossRef]
7. Spiering, H. Elastic interaction in spin-crossover compounds. In *Spin Crossover in Transition Metal Compounds III Topics in Current Chemistry*; Springer: Berlin/Heidelberg, Germany, 2004; Volume 235, pp. 171–195. [CrossRef]
8. Boukheddaden, K.; Linares, J.; Spiering, H.; Varret, F. One-dimensional Ising-like systems: An analytical investigation of the static and dynamic properties, applied to spin-crossover relaxation. *Eur. Phys. J. B* **2000**, *15*, 317–326. [CrossRef]
9. Boukheddaden, K.; Linares, J.; Varret, F. Thermodynamic properties of coupled mixed-valence molecules using a cooperative PKS theory: A second-order localized-delocalized transition. *Chem. Phys.* **1993**, *172*, 239–245. [CrossRef]
10. Constant-Machado, H.; Stancu, A.; Linares, J.; Varret, F. Thermal hysteresis loops in spin-crossover compounds analyzed in terms of classical Preisach model. *IEEE Trans. Mag.* **1998**, *34*, 2213–2219. [CrossRef]
11. Linares, J.; Jureschi, C.M.; Boukheddaden, K. Surface effects leading to unusual size dependence of the thermal hysteresis behavior in spin-crossover nanoparticles. *Magnetochemistry* **2016**, *2*, 24. [CrossRef]
12. Rotaru, A.; Linares, J.; Varret, F.; Codjovi, E.; Slimani, A.; Tanasa, R.; Enachescu, C.; Stancu, A.; Haasnoot, J. Pressure effect investigated with first-order reversal-curve method on the spin-transition compounds $[Fe_xZn_{1-x}(btr)_2(NCS)_2] \cdot H_2O$ (x = 0.6,1). *Phys. Rev. B* **2011**, *83*, 224107–224114. [CrossRef]
13. Qamar, O.A.; Cong, C.; Ma, H. Solid state mononuclear divalent nickel spin crossover complexes. *Dalton Trans.* **2020**, *49*, 17106–17114. [CrossRef] [PubMed]
14. Kahn, O. *Molecular Magnetism*; Wiley-VCH: New York, NY, USA, 1993.
15. Shepherd, H.J.; Bonnet, S.; Guionneau, P.; Bedoui, S.; Garbarino, G.; Nicolazzi, W.; Bousseksou, A.; Molnar, G. Pressure-induced two-step transition with structural symmetry breaking: X-ray diffraction, magnetic, and Ramman studies. *Phys. Rev. B* **2011**, *54*, 144107–144115. [CrossRef]
16. Krober, J.; Audière, J.P.; Claude, R.; Codjovi, E.; Kahn, O.; Hassnoot, J.; Grolière, F.; Jay, C.; Bousseksou, A.; Linares, J.; et al. Spin Transitions and Thermal Hysteresis in the Molecular-Based Materials [Fe(Htrz)2(trz)](BF4) and [Fe(Htrz)3](BF4)2.cntdot.H2O (Htrz = 1,2,4-4H-triazole; trz = 1,2,4-triazolato). *Chem. Mater.* **1994**, *6*, 1404–1412. [CrossRef]
17. Varret, F.; Slimani, A.; Boukheddaden, K.; Chong, C.; Mishra, H.; Collet, E.; Haasnoot, J.; Pillet, S. The Propagation of the Thermal Spin Transition of [Fe(Btr)2(NCS)2]_H2O Single Crystals Observed by Optical Microscopy. *New J. Chem.* **2011**, *35*, 2333–2340. [CrossRef]
18. Loutete-Dangui, E.D.; Codjovi, E.; Tokoro, H.; Dahoo, P.R.; Ohkoshi, S.; Boukheddaden, K. Spectroscopic ellipsometry investigations of the thermally induced first-order transition of RbMn[Fe(CN)6]. *Phys. Rev. B* **2008**, *78*, 014303–014312. [CrossRef]
19. Pillet, S.; Hubsch, J.; Lecomte, C. Single crystal diffraction analysis of the thermal spin conversion in $[Fe(btr)_2(NCS)_2](H_2O)$: Evidence for spin-like domain formation. *Eur. Phys. J. B* **2004**, *38*, 541–552. [CrossRef]
20. Roubeau, O.; Castro, M.; Burriel, R.; Haasnoot, J.G.; Reedijk, J. Calorimetric Investigation of Triazole-Bridged Fe(II) Spin-Crossover One-Dimensional Materials: Measuring the Cooperativity. *J. Phys. Chem. B* **2011**, *115*, 3003–3012. [CrossRef]
21. Rotaru, A.; Dîrtu, M.M.; Enachescu, C.; Tanasa, R.; Linares, J.; Stancu, A.; Garcia, Y. Calorimetric measurements of diluted spin crossover complexes $[Fe_xM_{1-x}(btr)_2(NCS)_2] \cdot H_2O$ with MII = Zn and Ni. *Polyhedron* **2009**, *28*, 2531–2536. [CrossRef]
22. Rotaru, A.; Varret, F.; Codjovi, E.; Boukheddaden, K.; Linares, J.; Stancu, A.; Guionneau, P.; Létard, J.F. Hydrostatic pressure investigation of the spin crossover compound [Fe(PM-BIA)2(NCS)2] polymorph I using reflectance detection. *J. Appl. Phys.* **2009**, *106*, 053515–053520. [CrossRef]
23. Rotaru, G.M.; Codjovi, E.; Dahoo, P.R.; Maurin, I.; Linares, J.; Rotaru, A. Monotoring-Spin-Crossover Properties by Diffussed Reflectivity. *Symmetry* **2021**, *13*, 1148. [CrossRef]
24. Wajnflasz, J.; Pick, R. Transitions "low spin"—"high spin" dans les complexes de Fe^{2+}. *J. Phys. Colloques* **1971**, *32*, 91–92. [CrossRef]
25. Bousseksou, A.; Nasser, J.; Linares, J.; Boukheddaden, K.; Varret, F. Ising-like model for the two-step spin-crossover. *J. Phys. I France* **1992**, *2*, 1381–1403. [CrossRef]

26. Linares, J.; Spiering, H.; Varret, F. Analytical solution of 1d ising-like systems modified by weak long-range interaction—Application to spin crossover compounds. *Eur. Phys. J. B* **1999**, *10*, 271–275. [CrossRef]
27. Chiruta, D.; Jureschi, C.-M.; Linares, J.; Dahoo, P.R.; Garcia, Y.; Rotaru, A. On the origin of multi-step spin transition behaviour in 1d nanoparticles. *Eur. Phys. J. B* **2015**, *88*, 233. [CrossRef]
28. Ndiaye, M.; Singh, Y.; Fourati, H.; Sy, M.; Lo, B.; Boukheddaden, K. Isomorphism between the electro-elastic modeling of the spin transition and Ising-like model with competing interactions: Elastic generation of self-organized spin states. *J. App. Phys.* **2021**, *129*, 153901–153921. [CrossRef]
29. Paez-Espejo, M.; Sy, M.; Boukheddaden, K. Elastic frustration causing two-step and multistep transitions in spin crossover solids: Emergence of complex Aantiferroelastic structures. *J. Am. Chem. Soc.* **2016**, *138*, 3202–3210. [CrossRef]
30. Shteto, I.; Linares, J.; Varret, F. Monte carlo entropic sampling for the study of metastable states and relaxation paths. *Phys. Rev. E* **1997**, *56*, 5128–5137. [CrossRef]
31. Linares, J.; Cazelles, C.; Dahoo, P.R.; Boukheddaden, K. A first-order phase transition studied by an Ising-like model solved by entropic Sampling Monte Carlo Method. *Symmetry* **2021**, *13*, 587. [CrossRef]
32. Linares, J.; Enachescu, C.; Boukheddaden, K.; Varret, F. Monte Carlo entropic sampling applied to spin crossover solids: The squareness of the thermal hysteresis loop. *Polyhedron* **2003**, *22*, 2453–2456. [CrossRef]
33. Constant-Machado, H.; Linares, J.; Varret, F.; Haasnoot, J.G.; Martin, J.P.; Zarembowitch, J.; Dworkin, A.; Bousseksou, A. Dilution effects in a spin crossover system, modelled in terms of direct and indirect intermolecular interactions. *J. Phys. I Fr.* **1996**, *6*, 1203–1216. [CrossRef]
34. Martin, J.P.; Zarembowitch, J.; Bousseksou, A.; Dworkin, A.; Haasnoot, J.G.; Varret, F. Solid State Effects on Spin Transitions: Magnetic, Calorimetric, and Moessbauer-Effect Properties of [$Fex Co_{1-x}$(4,4′-bis-1,2,4-triazole)$_2$$(NCS)_2$].cntdot.$H_2O$ Mixed-Crystal Compounds. *Inorg. Chem.* **1994**, *33*, 6325–6333. [CrossRef]